Title

To measure T1 of short T2 species using an inversion recovery prepared three-dimensional ultrashort echo time (3D IR-UTE) method: A phantom study

Authors

Wei, Zhao
Ma, Ya-Jun
Jang, Hyungseok
et al.

Publication Date

2020-05-01

DOI

10.1016/j.jmr.2020.106725

Peer reviewed

HHS Public Access

Author manuscript

J Magn Reson. Author manuscript; available in PMC 2021 May 01.

Published in final edited form as:

J Magn Reson. 2020 May ; 314: 106725. doi:10.1016/j.jmr.2020.106725.

To measure T_1 of short T_2 species Using an Inversion Recovery Prepared Three-Dimensional Ultrashort Echo Time (3D IR-UTE) Method: A Phantom Study

Zhao Wei[1,2,3], **Ya-Jun Ma**[1], **Hyungseok Jang**[1], **Wenhui Yang**[2,3], **Jiang Du**[1,*]

[1]Department of Radiology, University of California San Diego, CA, United States

[2]University of Chinese Academy of Sciences, Beijing, China

[3]Institute of Electrical Engineering, Chinese Academy of Sciences, Beijing, China

Abstract

Purpose—To demonstrate the feasibility of a new method for measuring T_1 of short T_2 species based on an adiabatic inversion recovery-prepared three-dimensional ultrashort echo time Cones (3D IR-UTE-Cones) sequence.

Methods—T_1 values for short T_2 species were quantified using 3D IR-UTE-Cones data acquired with different repetition times (TRs) and inversion times (TIs). An inversion efficiency factor Q was introduced into the fitting model to accurately calculate T_1 values for short T_2 species. Experiments were performed on twelve $MnCl_2$ aqueous solution phantoms with a wide range of T_1 values and T_2* values on a 3T clinical MR system to verify the efficacy of the proposed method. For comparison, a variable flip angle UTE (VFA-UTE) sequence, a variable TR UTE (VTR-UTE) sequence, and a conventional 2D IR fast spin echo (IR-FSE) sequence were also used to quantify T_1 values of those phantoms. T_1 values were compared between all performed sequences.

Results—The proposed 3D IR-UTE-Cones method provided higher contrast images of short T_2 phantoms and measured much shorter T_1 values than the 2D IR-FSE, VFA-UTE, and VTR-UTE methods. T_1 values as short as 2.95 ms could be measured by the 3D IR-UTE-Cones sequence. The 3D IR-UTE-Cones methods with different TRs were applied to different ranges of T_1 measurement, and the scan time was significantly decreased by using 5 TIs along the recovery curves to perform fitting with comparable accuracy.

Conclusion—The 3D IR-UTE-Cones sequence could accurately measure short T_1 values while providing high contrast images of short T_2 species.

*Corresponding Author: Jiang Du, Ph.D., jiangdu@ucsd.edu, University of California, San Diego, Department of Radiology, 200 West Arbor Drive, San Diego, CA 92103-8226, USA, Phone: (619) 471-0519 | Fax: (619) 471-0503.

Declaration of interests

The authors declare that they have no known competing financial interests or personal relationships that could have appeared to influence the work reported in this paper.

Graphical Abstract

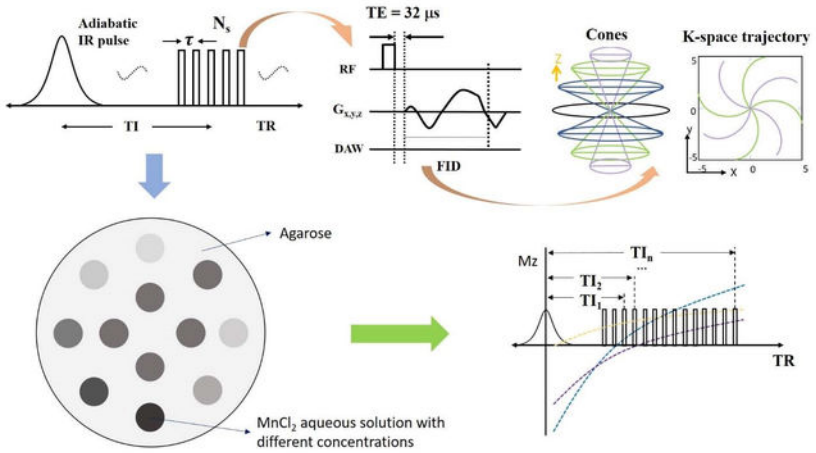

Keywords

adiabatic inversion recovery; UTE-Cones; T_1 measurement; $MnCl_2$ phantom

INTRODUCTION

Spin-lattice relaxation time (T_1) is an intrinsic MR tissue property. T_1 is also an important biomarker for many diseases, thus playing a key role in MR signal intensity and imaging contrast. For example, T_1 mapping of the brain can be used for the assessment of multiple sclerosis (MS) and Parkinson's disease [1–4]. Osteoarthritis (OA) can be detected at an early stage with T_1 mapping in delayed gadolinium-enhanced MRI of cartilage (dGEMRIC) [5, 6]. In nanoparticle-based hyperthermia, T_1 can be used as a biomarker to evaluate the concentration of iron-oxide nanoparticles (IONPs) [7–10]. In MRI-guided thermal ablation procedures, such as radiofrequency, laser, or focused ultrasound, T_1 mapping can be used to monitor the temperature [11–13].

A variety of T_1 measurement techniques have been reported, including inversion recovery (IR), Look-Looker (LL), variable flip angles (VFA), and variable repetition time (VTR)-based methods [14–18]. IR is the gold standard for T_1 measurement. The combinations of these methods with conventional spin echo (SE), fast spin echo (FSE), or gradient recalled echo (GRE) sequences have been used to measure T_1 values of primarily long T_2 species [1, 19–23], such as gray matter (GM), white matter (WM), cerebrospinal fluid (CSF), muscle, the superficial layers of articular cartilage, etc. However, for species with short T_2s, such as the deep layers of articular cartilage, menisci, tendons, ligaments, bone, and iron overload, their longitudinal magnetizations cannot be accurately rotated as their T_2s are around or shorter than the duration of the preparation (e.g., inversion or saturation) pulses [22]. The transverse magnetizations may decay significantly during the preparation pulses. Furthermore, conventional sequences may have too long echo times (TEs) to detect short T_2 signals. As a result, accurate T_1 mapping cannot be achieved for short T_2 species using conventional T_1 measurement methods.

Ultrashort echo time (UTE) based-methods are promising alternatives to overcome this problem. For example, the combination of variable flip angle (VFA) and UTE (VFA-UTE), variable TR and UTE (VTR-UTE), and adiabatic inversion recovery and UTE (IR-UTE) methods have been reported to provide accurate measurement of T_1 values of short T_2 species in the musculoskeletal (MSK) system [22,24–27]. VFA-UTE and VTR-UTE could provide volumetric T_1 mapping of short T_2 species, but they suffer from high sensitivity to B_1 inhomogeneity, with poor image contrast for short T_2 species. Adiabatic IR-UTE pulse sequences have been used for high contrast imaging of short T_2 species by suppressing signals from long T_2 species [27, 28]. The adiabatic IR-UTE method is able to provide not only high contrast morphological imaging but also quantitative evaluation, such as proton density (PD) and T_2* and T_1 mapping of short T_2 species [24, 25]. This is especially important since species with short T_2* values typically have short T_1 values, which are difficult or impossible to evaluate with conventional clinical sequences.

In this study, we aimed to develop a novel 3D IR-UTE based method to quantitatively measure T_1 values of short T_2* species. Data were acquired using an adiabatic inversion recovery prepared 3D UTE Cones (3D IR-UTE-Cones) sequence with a series of repetition times (TRs) and inversion times (TIs). An inversion efficiency factor Q was introduced to account for partial inversion of the longitudinal magnetization, and further incorporated into the fitting model for accurate T_1 mapping. Experiments were performed on twelve $MnCl_2$ aqueous solution phantoms with a wide range of T_1 values and T_2* values on a 3T clinical MR system to verify the efficacy of the proposed method.

THEORY and METHOD

Phantom Preparation

As reported in [29], the T_2* values of the $MnCl_2$ aqueous solutions had a linear relationship with their concentrations. Based on the linear relationship between concentrations and T_2* values, a wide range of concentrations of $MnCl_2$ aqueous solutions were made to explore the shortest T_1 values the proposed method could measure.

Twelve 5-mL polypropylene tubes filled with $MnCl_2$ aqueous solutions with concentrations ranging from 0 to 89.16 mM (details in Table 1) were placed inside a cylindrical container (8.5 cm in diameter, 9.5 cm in height) filled with agarose gel (1% by weight). During the scan, the tubes were aligned parallel to the B_0 field to minimize susceptibility artifact.

Pulse sequence and fitting model

The diagram of the 3D IR-UTE-Cones pulse sequence is illustrated in Figure 1 [30–32]. An adiabatic inversion recovery preparation pulse with a specific TI is followed by N number of spokes (Ns) separated with an equal time interval τ for fast data acquisition (Figure 1a). In this situation, TI is defined as the time from the center of the adiabatic inversion pulse to the center of the spoke cluster. A short rectangular pulse (duration of 26–52 μs) is used for non-selective signal excitation in each spoke (Figure 1b) followed by 3D spiral trajectories with conical view ordering (Figure 1c).

Adiabatic inversion pulses can effectively invert the longitudinal magnetizations of long T_2 species, while the longitudinal magnetizations of short T_2 species can only be partially inverted because of their fast decay during the relatively long adiabatic inversion process. To accurately describe the inversion status of species with different T_2s, we introduced an inversion efficiency factor Q with a range of −1 (full inversion, for species with long T_2s, e.g., T_2 > 100 ms) to 1 (no disturbance to the longitudinal magnetization, for species with extremely short T_2s, e.g., T_2 < 1 μs), and Q is 0 when the magnetization is completely saturated (for tissues with ultrashort T_2s, e.g., T_2 ~ 0.1 ms), as shown in Figure 1d.

Within a steady-state, the longitudinal magnetization of the N_s^{th} spoke is as follows:

$$S_z^{N_s} = K_{N_s} S_p + L_{N_s}, \tag{1}$$

Where

$$K_{N_s} = C_2[c_1\cos(\theta)]^{N_s}, \tag{2}$$

$$L_{N_s} = S_0(1 - C_2)[c_1\cos(\theta)]^{(N_s - 1)} + S_0(1 - c_1)\frac{1 - [c_1\cos(\theta)]^{N_s - 1}}{1 - c_1\cos(\theta)}, \tag{3}$$

And

$$S_p = \frac{QC_3L_{N_s}\cos(\theta) + S_0Q(1 - C_3)}{1 - QC_3K_{N_s}\cos(\theta)}. \tag{4}$$

In Equations (2)–(4), $c_1 = \exp(-\tau/T_1)$, which is related to the longitudinal T_1 relaxation during each spoke τ in the multi-spoke IR-UTE data acquisition; $C_2 = \exp\left[\tau^{(N_s - 1)}/2T_1\right]$, which is related to the longitudinal T_1 relaxation during the whole multi-spokes (Ns-1) τ; and C_3 = exp {– [TR – TI – τ(N_s – 1)/2]/T_1}, which is related to the longitudinal T_1 relaxation during the interval between the last spoke and next adiabatic IR pulse [TR – TI – τ(N_s – 1)/2]. S_0 is the steady-state magnetization, τ is the time interval between two spokes, and θ is the flip angle. S_p is the longitudinal magnetization after the adiabatic IR pulse. The explicit derivation of S_p can be found in appendix I.

As the UTE-Cones sequence can achieve echo time (TE) as short as 32 μs, which is much shorter than the T_2 of most species. Theoretically, the 3D IR-UTE-Cones sequence can detect signals from short T_2 species before they decay to near zero. According to Equations (1)–(4), when TR is kept constant and TIs are set incrementally along the recovery curve of the longitudinal magnetization, T_1 can be calculated by nonlinear fitting of equations (1)–(4).

Imaging Parameters

All sequences were implemented on a 3T clinical MRI scanner (MR750, GE Healthcare Technology, Milwaukee, WI) with maximum gradient amplitude of 50 mT/m and 200 T/m/s slew rate. An eight-channel transmit/receive knee coil was used for RF transmission and signal reception.

The 3D IR-UTE-Cones sequence used an adiabatic inversion pulse (Silver-Hoult with a pulse duration of 6.048 ms, a bandwidth of 1.643 kHz, and a maximum B_1 amplitude of 17 μT) for robust inversion. The duration of the hard RF pulse is 30 μs. As T_1 values of the phantoms distributed on a wide range, two TRs of 50 ms and 400 ms were used to compare the effects of different TRs. For each TR, we used a series of TR/TI combinations (for TR = 50 ms, TI = 8, 9, 10, 11, 12, 13, 14, 15, 16, 17, 18, 20, 24, 28, 32, 36, 40 ms; for TR = 400 ms, TI = 13, 15, 18, 25, 30, 40, 50, 70, 100, 130, 160, 200, 240, 280, 320, 360 ms). Other parameters were the same: TE = 32 μs; flip angle (FA) = 10°; field of view (FOV) = 120 × 120 × 128 mm^3; acquisition matrix size = 160 × 160 × 32; readout bandwidth = ± 125 kHz. Total scan times were about 145 min and 362 min, respectively.

For the purpose of comparison, the commonly used 2D IR-FSE sequence and two previously reported T_1 measurement methods (18, 21), UTE Cones-based variable flip angle (VFA-UTE) sequence and variable repetition time (VTR-UTE) sequence, were performed as well. To minimize the signal loss caused by fast T_2* decay, the shortest TE achievable for each sequence was selected. The parameters for 2D IR-FSE were: TE/TR = 6.52/4000 ms; FOV = 120 × 120 mm^2; slice thickness = 5 mm; matrix size = 192 × 192; readout bandwidth = ± 62.5 kHz; 13 TIs (TI = 50, 75, 100, 200, 300, 400, 600, 900, 1500, 2000, 2500, 3000, 3500 ms) were utilized for single slice imaging. The total scan time was about 30 min. Since both VFA-UTE and VTR-UTE are sensitive to the inhomogeneity of the transmitted B_1 field, the 3D dual TR UTE-Cones sequence was employed for actual flip angle imaging (AFI) and therefore B_1 field mapping. Parameters for AFI were: TE = 32 μs; TR = 20/100 ms; FOV = 120 × 120 × 128 mm^3; matrix size = 160 × 160 × 32; FA = 45°; bandwidth = ± 125 kHz; scan time was about 20 min. Parameters for VFA were: TE = 32 μs; TR = 20 ms; FOV = 120 × 120 × 128 mm^3; matrix size = 160 × 160 × 32; FA = 4°, 8°, 12°, 16°, 20°, 24°, 28°, 32°, 36°; bandwidth = ± 125 kHz; scan time was about 31 min. VTR-UTE used similar parameters except for the following changes: TR = 20, 40, 60, 80 ms; FA = 45°; scan time was about 34 min.

Furthermore, in order to estimate the range of T_2* values of phantoms, conventional 3D UTE-Cones acquisitions with 15 different TEs were executed. Parameters for T_2* measurement were: TE = 0.032, 0.2, 0.4, 0.8, 1.4, 2.2, 4.4, 6.6, 8.8, 11, 22, 33, 44, 66, 88 ms; TR = 100 ms; FOV = 120 × 120 × 128 mm^3; matrix size = 160 × 160 × 32; FA = 20°; bandwidth = ± 125 kHz; scan time was about 86 min.

Data Analysis

The data analysis algorithm was written in MATLAB (MathWorks, Natick, MA). Levenberg-Marquard method was used for nonlinear least-squares curve fitting and executed offline on DICOM images obtained by the protocols described above. Regions of interest

(ROIs) were placed in the center of each tube to avoid susceptibility artifacts near the interface. ROIs were then copied automatically to the corresponding site for all the images performed with different TIs at each TR. T_1 was calculated by nonlinear fitting of equations (1)–(4). The mean and standard deviation of T_1 were calculated for each tube. Linear regression analysis was performed between T_1 and $MnCl_2$ concentration for each method. The total scan time for the 3D IR-UTE-Cones method can be reduced by using a smaller number of TIs for each TR. We investigated the accuracy in T_1 estimation by using a smaller number of TIs, e.g., 5 vs. 16 or 17 TIs. Percent errors were calculated for each phantom by dividing the difference between the two T_1 values and the T_1 with more TIs, which was considered the reference standard.

RESULTS

Figure 2 displays representative images acquired with the 3D IR-UTE-Cones and 2D IR-FSE sequences with different TR/TI combinations. Tubes with higher $MnCl_2$ concentrations are “visible” with the 3D IR-UTE-Cones sequence but “invisible” with the 2D IR-FSE sequence with most TIs and TRs. In contrast, tubes with lower $MnCl_2$ concentrations (e.g., <= 0.24 mM) are more “visible” with the 2D IR-FSE sequence, and less “visible” with the 3D IR-UTE-Cones sequence, especially when a shorter TR of 50 ms is used. Tubes 7–12 were dark for all TIs with the 2D IR-FSE sequence, largely because of the high $MnCl_2$ concentrations and thus very short T_2* values (i.e., T_2*s were shorter than the TE of the 2D IR-FSE sequence). The 3D IR-UTE-Cones sequence captured signals of tubes with short T_2*s (tubes 7–12), which were undetectable (dark at any TI) with the 2D IR-FSE sequence. As a result, T_1 values of those tubes cannot be measured with the conventional 2D IR-FSE sequence but can be measured with the 3D IR-UTE-Cones sequence. Meanwhile, T_1 values of tubes with very low concentrations of $MnCl_2$ (e.g., tubes 1–3) can be measured with the 2D IR-FSE sequence but cannot be reliably measured with the 3D IR-UTE-Cones sequence, especially when a short TR (e.g., 50 ms) is used. The adiabatic IR pulse together with a short TR leads to efficient long T_2 suppression (27), precluding accurate quantification of T1s for phantoms with low concentrations of $MnCl_2$.

The averaged T_1 and T_2* values, as well as standard deviations of each tube calculated from different protocols, are listed in table 1. The dashes in table 1 indicate data using those specific settings were not suitable for fitting (too big fitting errors due to inappropriate imaging parameters, for example, too narrow range of TIs/TEs to measure long T_1 values/T_2* values). The 3D IR-UTE-Cones method could measure T_1 values as short as 2.95 ms, with corresponding T_2* values as short as 0.14 ms, which was unachievable with the other three methods.

Figure 3 shows the fitting curves of each tube with the 3D IR-UTE-Cones method. Two different TRs of 50 ms and 400 ms were investigated. Excellent fitting was achieved for tubes 4–12 with a TR of 50 ms, and tubes 1–10 with a TR of 400 ms. Less accurate fittings were achieved for tubes with lower $MnCl_2$ concentrations, and thus longer T_2* values, when a shorter TR of 50 ms and a narrower range of TIs of 8–40 ms were used. On the other hand, increased fitting errors were observed for tubes with high $MnCl_2$ concentrations when a longer TR of 400 ms and a broader range of TIs of 13–360 ms were used. A shorter TR and

narrower range of TIs are required for a more accurate estimation of extremely short T_1 values.

Figure 4 presents the linear fittings between the $MnCl_2$ concentration and the relaxivity rate R_1 ($1/T_1$) calculated by the 3D IR-UTE-Cones method. The R_1 values show strong correlations (R equaled to 0.99904 and 0.99995 for TR of 50 ms and 400 ms respectively) with the $MnCl_2$ concentrations, suggesting that the 3D IR-UTE-Cones method could reliably measure T_1 values, especially short T_1 values for phantoms with high $MnCl_2$ concentrations and thus short T_2* values.

Figure 5 shows nearly perfect correlations between $MnCl_2$ concentrations and R_1 values calculated from different methods, and correlations between the 3D IR-UTE-Cones and other methods (i.e., VTR-UTE, VFA-UTE, and IR-FSE) in terms of T_1 values. Those results demonstrate that the 3D IR-UTE-Cones method could accurately measure a broader range of T_1 values than the other three methods.

Table 2 shows the mean value and standard deviation of T_1 values calculated by fitting with 5 TIs at both TRs, and the T_1 percent errors between T_1 values calculated with 5 TIs and 16 TIs (when TR was 400 ms) or 17 TIs (when TR was 50 ms). Most of the percent errors were less than 5%, except for tubes 1 and 2 when TR was 400 ms (TR was too short to accurately calculate long T_1 values), tube 10 when TR was 400 ms (TR was too long to accurately calculate short T_1 values), and tubes 1–4 when TR was 50 ms (TR was too short to accurately calculate long T_1 values). The results demonstrated that five TIs were enough to calculate T_1 values accurately with the 3D IRUTE-Cones method when the parameters were appropriately set.

DISCUSSION

This phantom study demonstrated that the 3D IR-UTE-Cones method can be used as a valid method for T_1 measurement, especially for species with short T_2* values and short T_1 values. For phantoms with relatively long T_2* values and T_1 values, all four methods, including 2D IR-FSE, 3D VFA-UTE, 3D VTR-UTE, and 3D IR-UTE-Cones methods, provided similar results where excellent linear correlations were observed between T_1 relaxation rates (R_1s) and $MnCl_2$ concentrations. For phantoms with short T_2* values and short T_1 values, the 2D IR-FSE method was incapable of either imaging or T_1 quantification. Compared with 3D VFA-UTE and VTR-UTE methods, the 3D IR-UTE-Cones method produced a more accurate measurement of shorter T_1 values (phantoms with higher concentrations of $MnCl_2$). For the 3D IR-UTE-Cones method, the scan time was shortened by fitting with fewer TIs at an acceptable error (i.e., less than 5% error). However, the 3D IR-UTE-Cones method was not suitable for measuring long T_1 values, unless a very long TR was used at the cost of scan time. The method worked best for measuring short or extremely short T_1 values of short T_2 species.

Benefitting from the combination of the inversion recovery method and the 3D UTE-Cones acquisition scheme, the proposed 3D IR-UTE-Cones method provided both excellent imaging contrast and accurate measurement of T_1 values for phantoms with short T_2*

values. This was a significant advantage over the clinical 2D IR-FSE method, as well as the new 3D VFA-UTE and VTR-UTE methods. The echo time of the 3D UTE-Cones sequence is as short as 32 μs, which was short enough to capture signals from short T_2* phantoms (e.g., T_2* of 0.14 ms for tube 12), as shown in Table 1. On the other hand, for the clinical 2D IR-FSE sequence, the shortest echo time was 6.52 ms, during which the signals from tubes 6 to 12 had completely decayed. Previously reported 3D UTE-Cones-based VFA and VTR methods have drawbacks, such as high sensitivity to the B_1 field inhomogeneity [26] and poor image contrast for short T_2 species. Both VFA and VTR methods need to be combined with AFI to do B_1 correction, but one of the fundamental assumptions which general AFI relies on is that the two TRs (a shorter TR1 and a longer TR2) are much shorter than the T_1 [33]. TRs for the AFI-VFA-UTE-Cones and AFI-VTR-UTE-Cones protocols could not satisfy the condition TR << T_1 values when the T_1 values were very short. Consequently, the ultrashort T_1 values of tube 9 to 11 were unable to be measured with these two methods. Furthermore, the fitting model of the proposed 3D IR-UTE-Cones method introduced an inversion recovery efficiency factor Q, which describes the inversion status of tissues with different T_2* values more precisely than conventional SE- and GRE-based IR methods, making the measured short T_1 values of short T_2* species more accurate.

The 3D IR-UTE-Cones method also provided high contrast images for short T_2 species, another significant advantage over the other three methods. In 3D IR-UTE-Cones imaging, long T_2 and long T_1 species were excellently suppressed, especially when a shorter TR was used, providing excellent contrast for short T_2 species. The short T_2 species appear with much reduced image contrast with both VFA-UTE and VTR-UTE due to the high signals from species with longer T_1 and T_2 values. The advantage of the 3D IR-UTE-Cones method in terms of high contrast imaging is even more obvious for short T_2 species, such as cortical bone, as these species are nearly “invisible” to both VFA-UTE and VTR-UTE imaging due to their low proton density and short T_2*, resulting in much lower signal than the surrounding species which have higher proton densities and longer T_2s, such as muscle and marrow fat.

As shown in Table 1 and Figure 3, TR plays an important role in the accurate quantification of T_1 relaxation when using the 3D IR-UTE-Cones method. The general rule is that a longer TR is preferred for more accurate quantification of longer T_1s, while a shorter TR is preferred for more accurate quantification of shorter T_1s. When the T_1 is much longer than the TR, the fitting is unreasonable and the resulting T_1 value is deemed unacceptable due to the considerable fitting error. The nulling points of the fitting curves of tubes 1–3 should be greater than the curves of tubes 4–12 in Figure 3(a) and the nulling point of the fitting curve of tube 1 should be greater than tubes 2–12 in Figure 3(b), indicating that the TRs of 50 ms and 400 ms were inappropriate for T_1 measurements of tubes 1–3 and tube 1, respectively. When the T_1 is much shorter than the TR, measurement with a relatively long TR would be inaccurate, as well. As shown in Figure 3(b), the data sample points of tubes 11–12 deviated significantly from the fitting curves, which resulted in large fitting errors and unreasonable fitting results, illustrating that the data acquired with a long TR of 400 ms were not suitable for short T_1 calculations. In IR-UTE imaging, long T_2 signals will be suppressed more efficiently by using a shorter TR (e.g., 50 ms in this study) (27). Tubes 4–5 have relatively long T_2*s of 10.61 and 4.99 ms, respectively, as shown in Table 1. The IR pulse will

partially invert their longitudinal magnetizations as the duration of the adiabatic IR pulse is on the order of their T_2*s [27, 34]. When a short TR (e.g., 50 ms) is used, tubes 4–5 show as low signal in 3D IR-UTE-Cones imaging, leading to increased errors in T_1 quantification. A longer TR (e.g., 400 ms) is expected to provide more accurate T_1 quantification for tubes 4–5, consistent with results shown in Tables 1 and 2. A longer T_1 means much increased scan time with the 3D IR-UTE-Cones method. Furthermore, tissues with longer T_1s may also be imaged and quantified with conventional clinical sequences. And thus the 3D IR-UTE-Cones method is of less importance. On the other hand, tissues with very short T_1s, such as iron overload in the liver or spine [35, 36], or hemosiderin in the hemophilia joint [37], cannot be imaged and quantified with conventional clinical sequences. The 3D IR-UTE-Cones sequence with a longer TR (e.g, 400 ms) may not work well when the iron concentration is too high and T_2* too short (e.g., T_2* < 0.3 ms). In such cases, a shorter TR (e.g., 50 ms) is expected to work better, providing more accurate quantification of T_1 relaxation. Consequently, the 3D IR-UTE-Cones method based on short TRs is extremely suitable for short T_1 measurements of short T_2 species. However, the shortest TR is limited by the acceptable specific absorption ratio (SAR).

With the advantage of being able to measure short T_1 values of short T_2 species, the proposed 3D IR-UTE-Cones method could be promising in a variety of applications. For instance, as the accumulation of iron shortens both T_1 and T_2* values of local tissue, T_1 could be used as a biomarker of iron overload, both spatially (location) and quantitatively (concentration). In several pathologies, accumulation of iron occurs after frequent blood transfusions or in the case of excess iron absorption [38, 39]. Recently, quantitative susceptibility mapping (QSM) was supposed to quantify the liver iron concentration (LIC), but the QSM and LIC only showed correlation at low LIC levels [35, 40]. The 3D IR-UTE-Cones method can be used to quantify LIC with T1 mapping at high LIC levels. Similarly, the presence of hemorrhage modulates T_1 and T_2 values. T_2 values have previously been used to identify hemorrhage [41]; analogously, T_1 mapping could be used as a probe for hemorrhage detection. The proposed 3D IR-UTE-Cones T_1 mapping might therefore be a useful method. In the iron oxide nanoparticles (IONPs)-based hyperthermia therapy and stem cell therapy, the 3D IR-UTE-Cones method could be utilized to visualize the locations and concentrations of the IONPs or labeled stem cells with T_1 mapping [10, 42]. One of our recent studies showed that the iron accumulation in the cartilage of hemophilic populations decreased T_2* values of cartilage [37], presenting another potential application of the proposed 3D IR-UTE-Cones T_1 measurement method.

This study has several limitations. First, we have only demonstrated the technical feasibility of the 3D IR-UTE-Cones method in measuring short T_1 values of short T_2* species by studying $MnCl_2$ aqueous solution phantoms. No ex vivo or in vivo experiments were completed in this study. Second, the efficiency and accuracy of the 3D IR-UTE-Cones protocol in terms of signal-to-noise ratio (SNR) and contrast-to-noise ratio (CNR) were not assessed or compared with the other three T_1 measurement methods mentioned above. However, it is quite obvious that the 3D IR-UTE-Cones method provides improved CNR for phantoms with high $MnCl_2$ concentrations over 2D IR-FSE, VFA-UTE, and VTR-UTE methods. Third, Nss were set to 1 for both TRs, and the number of TIs along each inversion recovery curve for a TR of 50 ms and 400 ms were set to 17 and 16, respectively. These

were the main reason for the long total scan time. Multi-spoke acquisitions (e..g, Ns of more than 30) and fewer TIs could be used in future study to reduce the scan time. Fourth, as there are many potential clinical applications, such as iron quantification in diseases like hemophilia, thalassemia, liver diseases, etc., and T_1 mapping for cortical bone, ligaments, tendons, etc., clinical evaluation of this novel technique remains to be done.

CONCLUSION

In this study, we demonstrated the feasibility of using the inversion recovery-prepared 3D ultrashort echo time Cones sequence to accurately measure short T_1 values while providing high contrast images of short T_2 species.

Supplementary Material

Refer to Web version on PubMed Central for supplementary material.

ACKNOWLEDGEMENTS

The authors achknowledge grant support from the GE Healthcare, NIH (2R01 AR062581, 1R01 NS092650, and 1R01 AR068987) and the scholarship support from the Joint PhD Training Program of University of Chinese Academy of Sciences (UCAS).

REFERENCE

[1]. Vrenken H, Geurts JJG, Knol DL, Noor Van Dijk L, Dattola V, Jasperse B, Van Schijndel RA, Polman CH, Castelijns JA, Barkhof F, Pouwels PJW, Whole-brain T1 mapping in multiple sclerosis: Global changes of normal-appearing gray and white matter, Radiology. 240 (2006) 811–820. 10.1148/radiol.2403050569. [PubMed: 16868279]

[2]. Manfredonia F, Ciccarelli O, Khaleeli Z, Tozer DJ, Sastre-Garriga J, Miller DH, Thompson AJ, Normal-appearing brain T1 relaxation time predicts disability in early primary progressive multiple sclerosis, Arch. Neurol. 64 (2007) 411–415. 10.1001/archneur.64.3.411. [PubMed: 17353385]

[3]. Papadopoulos K, Tozer DJ, Fisniku L, Altmann DR, Davies G, Rashid W, Thompson AJ, Miller DH, Chard DT, TI-relaxation time changes over five years in relapsing-remitting multiple sclerosis, Mult. Scler 16 (2010) 427–433. 10.1177/1352458509359924. [PubMed: 20086026]

[4]. Baudrexel S, Nürnberger L, Rüb U, Seifried C, Klein JC, Deller T, Steinmetz H, Deichmann R, Hilker R, Quantitative mapping of T1 and T2 discloses nigral and brainstem pathology in early Parkinson's disease, Neuroimage. 51 (2010) 512–520. 10.1016/j.neuroimage.2010.03.005. [PubMed: 20211271]

[5]. Tiderius CJ, Olsson LE, Leander P, Ekberg O, Dahlberg L, Delayed gadolinium-enhanced MRI of cartilage (dGEMRIC) in early knee osteoarthritis, Magn. Reson. Med. 49 (2003) 488–492. 10.1002/mrm.10389. [PubMed: 12594751]

[6]. Burstein D, Velyvis J, Scott KT, Stock KW, Kim YJ, Jaramillo D, Boutin RD, Gray ML, Protocol issues for delayed Gd(DTPA)2--enhanced MRI (dGEMRIC) for clinical evaluation of articular cartilage, Magn. Reson. Med. 45 (2001) 36–41. 10.1002/1522-2594(200101)45:1<36::AID-MRM1006>3.0.CO;2-W. [PubMed: 11146483]

[7]. Mahmoudi K, Bouras A, Bozec D, Ivkov R, Hadjipanayis C, Magnetic hyperthermia therapy for the treatment of glioblastoma: a review of the therapy's history, efficacy and application in humans, Int. J. Hyperth. 34 (2018) 1316–1328. 10.1080/02656736.2018.1430867.

[8]. Zhang J, Chamberlain R, Etheridge M, Idiyatullin D, Corum C, Bischof J, Garwood M, Quantifying iron-oxide nanoparticles at high concentration based on longitudinal relaxation using a three-dimensional SWIFT look-locker sequence, Magn. Reson. Med. 71 (2014) 1982–1988. 10.1002/mrm.25181. [PubMed: 24664527]

[9]. Lv YB, Chandrasekharan P, Li Y, Liu XL, Avila JP, Yang Y, Chuang KH, Liang XJ, Ding J, Magnetic resonance imaging quantification and biodistribution of magnetic nanoparticles using: T1-enhanced contrast, J. Mater. Chem. B. 6 (2018) 1470–1478. 10.1039/c7tb03129g. [PubMed: 32254211]

[10]. Vallabani NVS, Singh S, Recent advances and future prospects of iron oxide nanoparticles in biomedicine and diagnostics, 3 Biotech. 8 (2018) 1–23. 10.1007/s13205-018-1286-z.

[11]. Woodrum DA, Kawashima A, Gorny KR, Mynderse LA, Prostate cancer: state of the art imaging and focal treatment, Clin. Radiol. 72 (2017) 665–679. 10.1016/j.crad.2017.02.010. [PubMed: 28385253]

[12]. Kuroda K, MR techniques for guiding high-intensity focused ultrasound (HIFU) treatments, J. Magn. Reson. Imaging. 47 (2018) 316–331. 10.1002/jmri.25770. [PubMed: 28580706]

[13]. Zhu M, Sun Z, Ng CK, Image-guided thermal ablation with MR-based thermometry, Quant. Imaging Med. Surg. 7 (2017) 356–368. 10.21037/qims.2017.06.06. [PubMed: 28812002]

[14]. Deoni SCL, Rutt BK, Peters TM, Rapid combined T1 and T2 mapping using gradient recalled acquisition in the steady state, Magn. Reson. Med. 49 (2003) 515–526. 10.1002/mrm.10407. [PubMed: 12594755]

[15]. Techawiboonwong A, Song HK, Leonard MB, Wehrli FW, Cortical Bone Water : In Vivo Quantification with Ultrashort Echo-Time MRI Imaging, Radiology. 248 (2008).

[16]. Cheng H-LM, Wright GA, Rapid High-Resolution T1 mapping by Variable Flip Angles: Accurable and Precise Measurements in the Presence of Radiofrequency field Inhomogeneity, Magn. Reson. Med. 55 (2006) 566–574. 10.1002/mrm.20791. [PubMed: 16450365]

[17]. Stikov N, Boudreau M, Levesque IR, Tardif CL, Barral JK, Pike GB, On the accuracy of T1 mapping: Searching for common ground, Magn. Reson. Med. 73 (2015) 514–522. 10.1002/mrm.25135. [PubMed: 24578189]

[18]. Chen J, Chang EY, Carl M, Ma Y, Shao H, Chen B, Wu Z, Du J, Measurement of bound and pore water T1 relaxation times in cortical bone using three-dimensional ultrashort echo time cones sequences, Magn. Reson. Med. 77 (2017) 2136–2145. 10.1002/mrm.26292. [PubMed: 27263994]

[19]. Zaharchuk G, Martin AJ, Rosenthal G, Manley GT, Dillon WP, Measurement of cerebrospinal fluid oxygen partial pressure in humans using MRI, Magn. Reson. Med. 54 (2005) 113–121. 10.1002/mrm.20546. [PubMed: 15968660]

[20]. Marty B, Carlier PG, Physiological and pathological skeletal muscle T1 changes quantified using a fast inversion-recovery radial NMR imaging sequence, Sci. Rep. 9 (2019) 1–9. 10.1038/s41598-019-43398-x. [PubMed: 30626917]

[21]. Marty B, Coppa B, Baudin P, Carlier P, Monitoring skeletal muscle chronic fatty degenerations using fast NMR T1-mapping, Neuromuscul. Disord. 27 (2017) S126–S127. 10.1016/j.nmd.2017.06.128.

[22]. Ma YJ, Zhao W, Wan L, Guo T, Searleman A, Jang H, Chang EY, Du J, Whole knee joint T 1 values measured in vivo at 3T by combined 3D ultrashort echo time cones actual flip angle and variable flip angle methods, Magn. Reson. Med. 81 (2019) 1634–1644. 10.1002/mrm.27510. [PubMed: 30443925]

[23]. Nieminen MT, Rieppo J, Silvennoinen J, Töyräs J, Hakumäki JM, Hyttinen MM, Helminen HJ, Jurvelin JS, Spatial assessment of articular cartilage proteoglycans with Gd-DTPA-enhanced T1 imaging, Magn. Reson. Med. 48 (2002) 640–648. 10.1002/mrm.10273. [PubMed: 12353281]

[24]. Du J, Carl M, Bydder M, Takahashi A, Chung CB, Bydder GM, Qualitative and quantitative ultrashort echo time (UTE) imaging of cortical bone, J. Magn. Reson. 207 (2010) 304–311. 10.1016/j.jmr.2010.09.013. [PubMed: 20980179]

[25]. Du J, Carl M, Bae WC, Statum S, Chang EY, Bydder GM, Chung CB, Dual inversion recovery ultrashort echo time (DIR-UTE) imaging and quantification of the zone of calcified cartilage (ZCC), Osteoarthr. Cartil. 21 (2013) 77–85. 10.1016/j.joca.2012.09.009. [PubMed: 23025927]

[26]. Ma YJ, Lu X, Carl M, Zhu Y, Szeverenyi NM, Bydder GM, Chang EY, Du J, Accurate T 1 mapping of short T 2 tissues using a three-dimensional ultrashort echo time cones actual flip angle imaging-variable repetition time (3D UTE-Cones AFI-VTR) method, Magn. Reson. Med. 80 (2018) 598–608. 10.1002/mrm.27066. [PubMed: 29314235]

[27]. Ma YJ, Chen Y, Li L, Cai Z, Wei Z, Jerban S, Jang H, Chang EY, Du J, Trabecular bone imaging using a 3D adiabatic inversion recovery prepared ultrashort TE Cones sequence at 3T, Magn. Reson. Med. (2019) 1–12. 10.1002/mrm.28027.

[28]. Jang H, Wei Z, Wu M, Ma YJ, Chang EY, Corey-Bloom J, Du J, Improved volumetric myelin imaging in human brain using 3D dual echo inversion recovery-prepared UTE with complex echo subtraction, Magn. Reson. Med. (2019) 1–10. 10.1002/mrm.28082.

[29]. Kurmis AP, Barber C, Slavotinek JP, A MnCl2-based MR Signal Intensity Linear Response Phantom, Radiol. Technol. 79 (2007) 119–125. [PubMed: 18032749]

[30]. Ma YJ, Zhu Y, Lu X, Carl M, Chang EY, Du J, Short T 2 imaging using a 3D double adiabatic inversion recovery prepared ultrashort echo time cones (3D DIR-UTE-Cones) sequence, Magn. Reson. Med. 79 (2018) 2555–2563. 10.1002/mrm.26908. [PubMed: 28913879]

[31]. Carl M, Bydder GM, Du J, UTE imaging with simultaneous water and fat signal suppression using a time-efficient multispoke inversion recovery pulse sequence, Magn. Reson. Med. 76 (2016) 577–582. 10.1002/mrm.25823. [PubMed: 26309221]

[32]. Gurney PT, Hargreaves BA, Nishimura DG, Design and analysis of a practical 3D cones trajectory, Magn. Reson. Med. 55 (2006) 575–582. 10.1002/mrm.20796. [PubMed: 16450366]

[33]. Yarnykh VL, Actual flip-angle imaging in the pulsed steady state: A method for rapid three-dimensional mapping of the transmitted radiofrequency field, Magn. Reson. Med. 57 (2007) 192–200. 10.1002/mrm.21120. [PubMed: 17191242]

[34]. Larson PEZ, Conolly SM, Pauly JM, Nishimura DG, Using adiabatic inversion pulses for long-T2 suppression in ultrashort echo time (UTE) imaging, Magn. Reson. Med. 58 (2007) 952–961. 10.1002/mrm.21341. [PubMed: 17969119]

[35]. Lin H, Wei H, He N, Fu C, Cheng S, Shen J, Wang B, Yan X, Liu C, Yan F, Quantitative susceptibility mapping in combination with water-fat separation for simultaneous liver iron and fat fraction quantification, Eur. Radiol. 28 (2018) 3494–3504. 10.1007/s00330-017-5263-4. [PubMed: 29470640]

[36]. Hanrahan CJ, Shah LM, MRI of spinal bone marrow: Part 2, T1-weighted imaging-based differential diagnosis, Am. J. Roentgenol. 197 (2011) 1309–1321. 10.2214/AJR.11.7420. [PubMed: 22109284]

[37]. von Drygalski A, Barnes RFW, Jang H, Ma Y, Wong JH, Berman Z, Du J, Chang EY, Advanced magnetic resonance imaging of cartilage components in haemophilic joints reveals that cartilage hemosiderin correlates with joint deterioration, Haemophilia. 25 (2019) 851–858. 10.1111/hae.13802. [PubMed: 31199035]

[38]. St. Pierre TG, Clark PR, Chua-Anusorn W, Measurement and mapping of liver iron concentrations using magnetic resonance imaging, Ann. N. Y. Acad. Sci. 1054 (2005) 379–385. 10.1196/annals.1345.046. [PubMed: 16339686]

[39]. Berdoukas V, Chouliaras G, Moraitis P, Zannikos K, Berdoussi E, Ladis V, The efficacy of iron chelator regimes in reducing cardiac and hepatic iron in patients with thalassaemia major: A clinical observational study, J. Cardiovasc. Magn. Reson. 11 (2009). 10.1186/1532-429X-11-20.

[40]. Sharma SD, Fischer R, Schoennagel BP, Nielsen P, Kooijman H, Yamamura J, Adam G, Bannas P, Hernando D, Reeder SB, MRI-based quantitative susceptibility mapping (QSM) and R2* mapping of liver iron overload: Comparison with SQUID-based biomagnetic liver susceptometry, Magn. Reson. Med. 78 (2017) 264–270. 10.1002/mrm.26358. [PubMed: 27509836]

[41]. Ghugre NR, Ramanan V, Pop M, Yang Y, Barry J, Qiang B, Connelly KA, Dick AJ, Wright GA, Quantitative tracking of edema, hemorrhage, and microvascular obstruction in subacute myocardial infarction in a porcine model by MRI, Magn. Reson. Med. 66 (2011) 1129–1141. 10.1002/mrm.22855. [PubMed: 21337425]

[42]. Haedicke IE, Loai S, Cheng HLM, An efficient T1 contrast agent for labeling and tracking human embryonic stem cells on MRI, Contrast Media Mol. Imaging. 2019 (2019) 1–11. 10.1155/2019/3475786.

- Capable of quantifying the T1 of short T2 species;
- Can measure T1 as short as 2.95 ms;
- Introduce an inversion efficiency factor Q to accurately measure a wide range of T1.

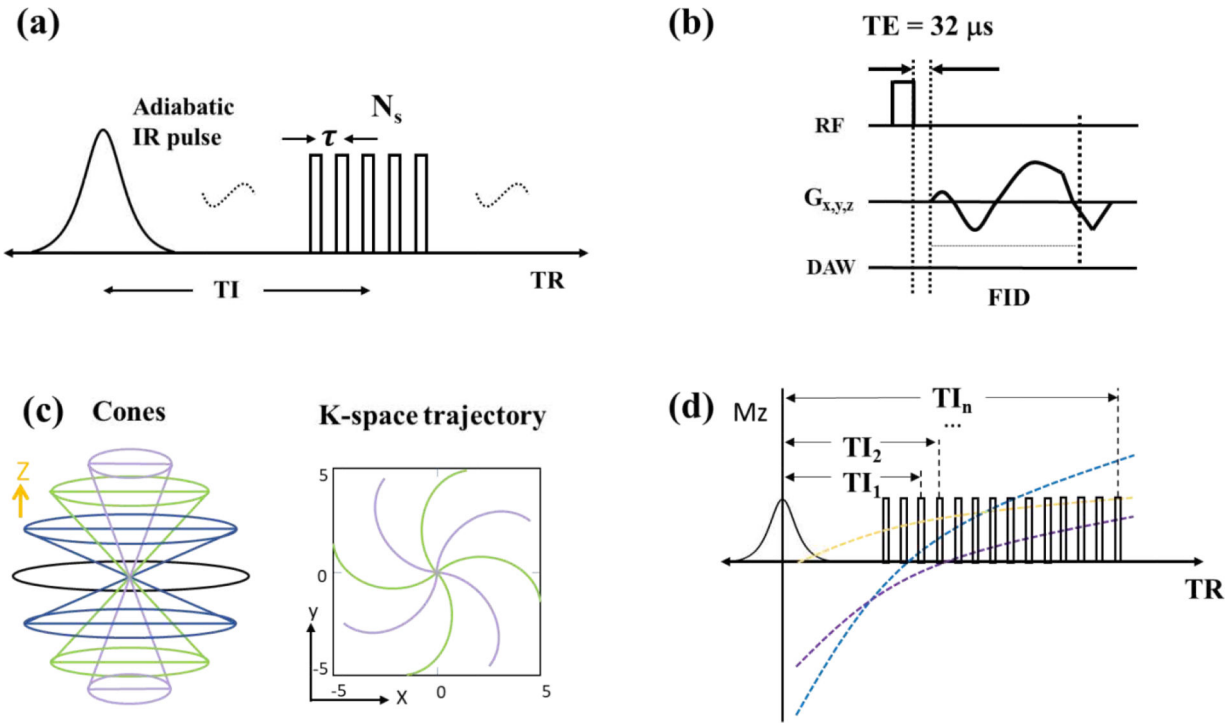

Figure 1.

3D IR-UTE-Cones sequence diagram for T_1 measurement. (a) The pulse sequence scheme showing an adiabatic inversion preparation pulse followed by a 3D UTE-Cones data acquisition. (b) In the basic 3D UTE-Cones sequence, a rectangular pulse is used for signal excitation followed by 3D spiral sampling with TE of 32 μs. (c) Conical view ordering of the spiral trajectories. (d) Longitudinal magnetization scheme of three representative tissues (yellow, tissues with ultrashort T_2* saturated during the IR pulse; blue, tissues with short T_2* partially inverted during the IR pulse; purple, tissues with long T_2* fully inverted during the IR pulse) during the course of inversion recovery.

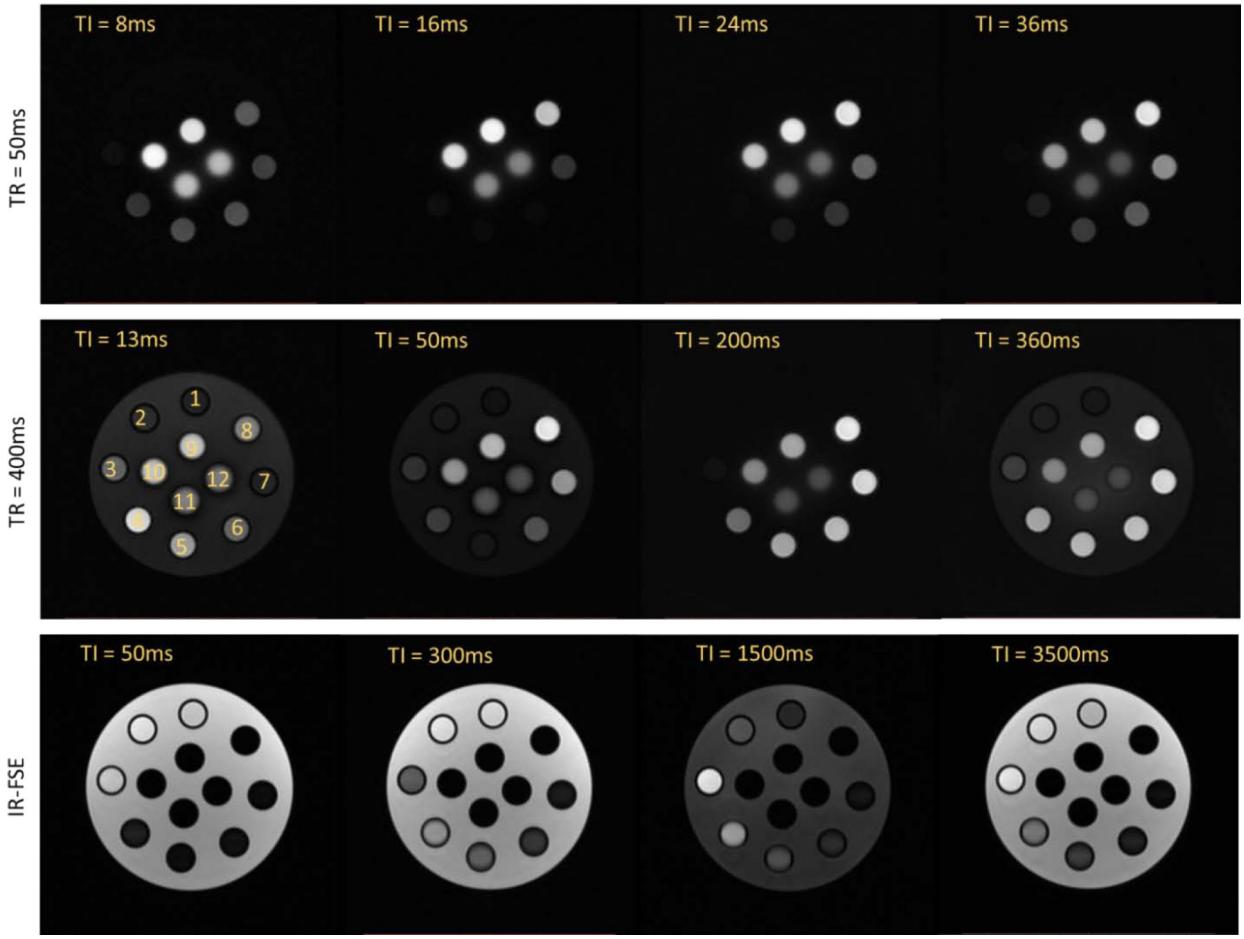

Figure 2.

Images acquired with 3D IR-UTE-Cones and 2D IR-FSE sequences. The first and middle row are representative images acquired with the 3D IR-UTE protocol at different TR/TI combinations: TR/TI = 50/8, 16, 24, and 36 ms (first row), TR/TI = 400/13, 50, 200, and 360 ms (middle row). The bottom row shows the images acquired with the 2D IR-FSE protocol at TR/TI = 4000/50, 300, 1500, and 3500 ms. The numbers of the tubes are labeled on the first image of the middle row.

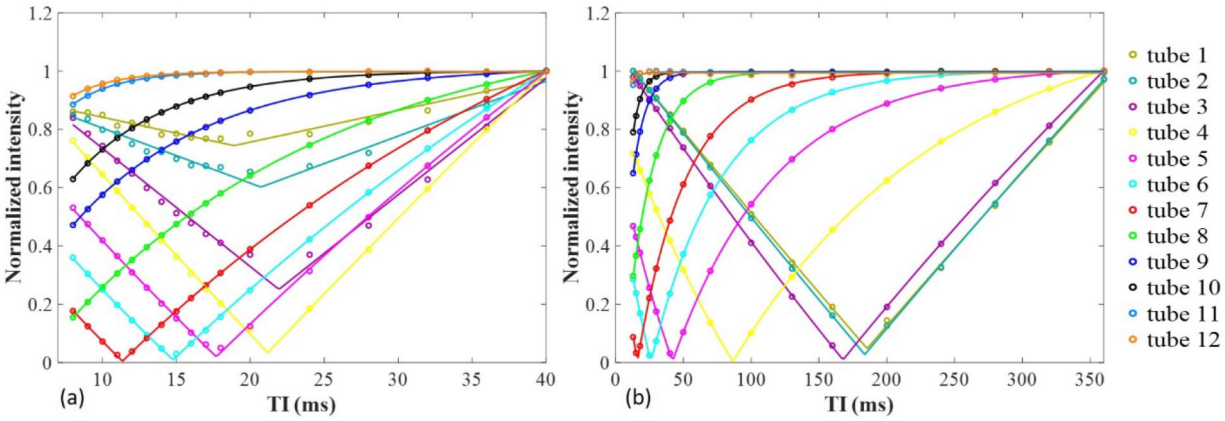

Figure 3.

The fitting curves of each tube under the 3D IR-UTE-Cones method. (a) The fitting curves of the TR = 50 ms set. (b) The fitting curves of the TR = 400 ms set.

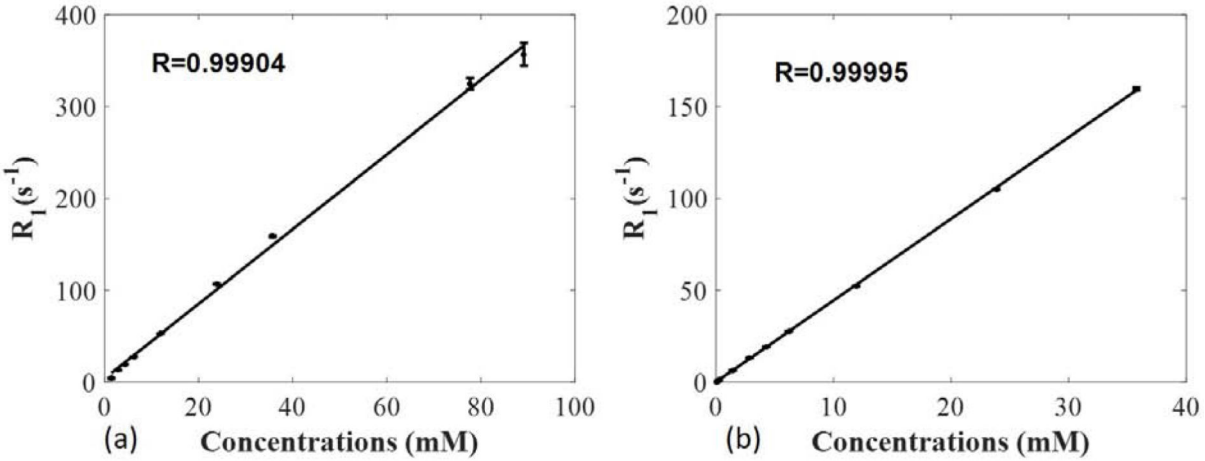

Figure 4.

The correlations between the R_1 values calculated using the 3D IR-UTE-Cones method and $MnCl_2$ solution concentrations. (a) The correlation between R_1 values from TR = 50 ms set (tube 4–12) and concentrations. (b) The correlation between R_1 values from TR = 400 ms set (tube 1–10) and concentrations.

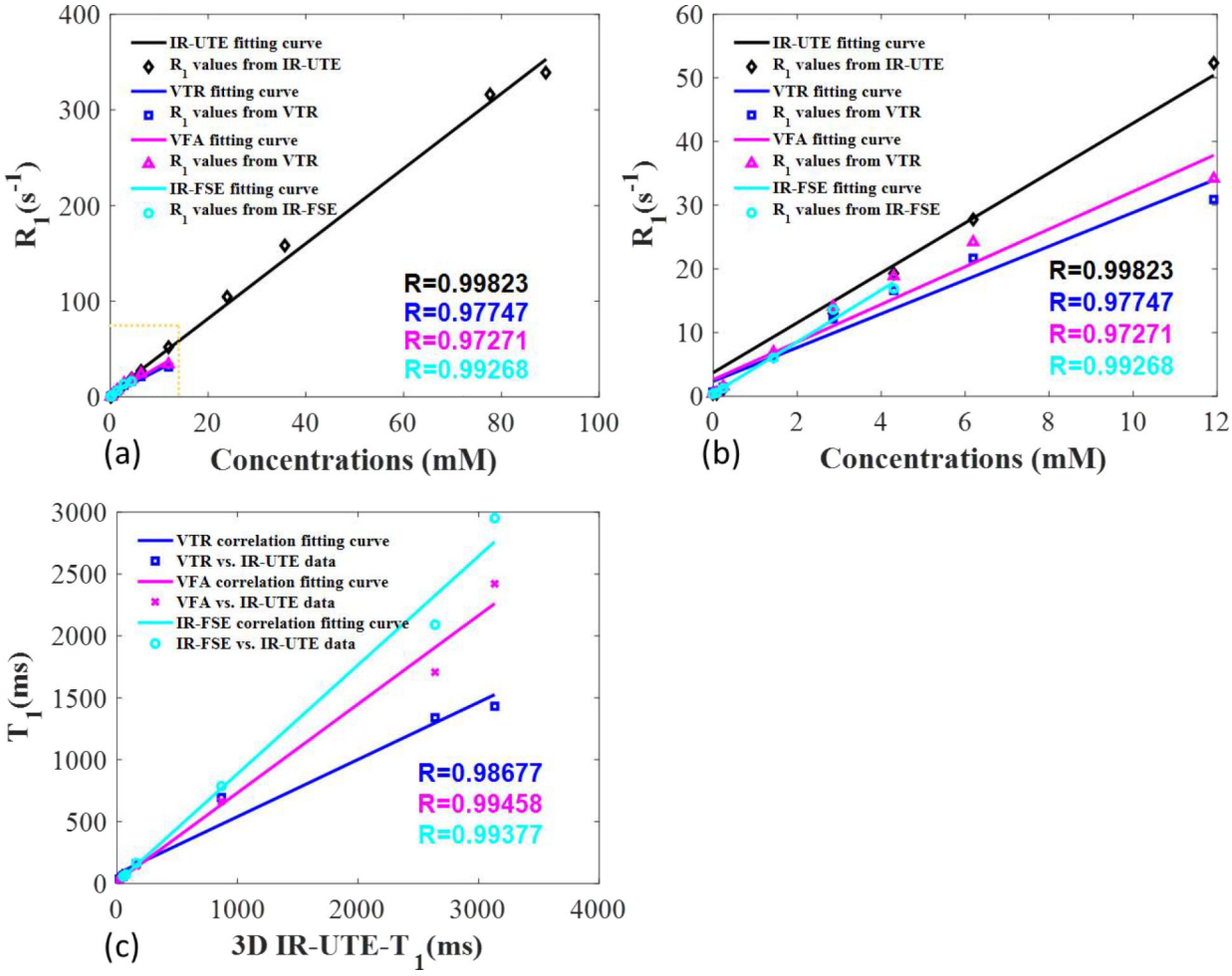

Figure 5.

Correlations between R_1s obtained from different methods and $MnCl_2$ solution concentrations and the correlations between the 3D IR-UTE-Cones method and other methods. (a) The correlations between R_1s obtained from 3D IR-UTE-Cones, VTR-UTE, VFA-UTE, and IR-FSE and $MnCl_2$ solution concentrations. (b) The enlargement of the region marked with a yellow dashed line in (a). (c) The correlations between T_1 values calculated by 3D IR-UTE-Cones and VTR-UTE, VFA-UTE, and 2D IR-FSE.

Table 1.

T_2* and T_1 results of different imaging protocols

Tube Numbers	Concentration (mM)	T_2* (ms)	Estimated T_1 values (ms)				
			3D IR-UTE (TR = 400 ms)	3D IR-UTE (TR = 50 ms)	VFA-UTE	VTR-UTE	IR-FSE
1	0	-	3133.23±794.74	-	2418.00±148.26	1433.08±487.12	2953.34±16.86
2	0.08	-	2639.91±304.17	-	1710.69±98.14	1337.63±334.19	2092.08±3.51
3	0.24	-	863.31±20.15	-	662.89±32.35	695.72±25.30	782.66±1.08
4	1.43	10.61±0.42	158.43±0.48	231.34±39.83	143.56±71.32	159.93±4.03	166.52±0.49
5	2.86	4.99±0.16	76.53±0.14	90.09±6.84	71.32±14.65	82.55±2.42	73.13±14.65
6	4.29	3.44±0.11	51.86±0.15	58.29±2.43	53.29±3.36	60.23±1.97	59.33±2.34
7	6.20	2.34±0.05	36.08±0.09	37.56±0.64	41.23±3.01	46.26±1.96	-
8	11.92	1.16±0.03	19.09±0.07	18.88±0.03	29.27±3.95	32.33±3.07	-
9	23.84	0.55±0.02	9.55±0.58	9.39±0.01	-	-	-
10	35.76	0.35±0.02	6.33±0.13	6.31±0.01	-	-	-
11	77.72	0.16±0.02	-	3.17±0.04	-	-	-
12	89.16	0.14±0.03	-	2.95±0.07	-	-	-

Table 2.

T_1 values calculated by fitting with five TIs under 3D IR-UTE-Cones method.

Tube Numbers	TR = 400 ms		TR = 50 ms	
	T_1_5 (ms)[a]	Percent Error (%)[b]	T_1_5 (ms)[a]	Percent Error (%)[b]
1	5252.08±1423.90	67.63%	-	-
2	3173±628.66	20.20%	-	-
3	847.94±57.16	1.78%	-	-
4	159.07±2.23	0.40%	181.22±1.74	21.67%
5	76.59±0.31	0.08%	87.6±3.19	2.76%
6	51.87±0.33	0.02%	55.53±0.22	4.73%
7	37.03±0.05	2.63%	37.21±0.88	0.93%
8	19.10±2.87	0.05%	18.98±0.03	0.53%
9	9.68±0.55	1.36%	9.41±0.01	0.21%
10	6.86±2.26	8.37%	6.32±0.01	0.16%
11	-	-	3.16±0.10	0.32%
12	-	-	2.99±0.24	1.36%

[a] T_1_5 represents the T_1 values calculated with five TIs at both TRs (TR/TI = 50 / 8, 12, 16, 24, 40 ms; TR/TI = 400 / 13, 40, 130, 240, 360 ms).

[b] Percent Error represents the T_1_5 value errors compared with T_1 values calculated with 16 TIs when TR = 400 ms and 17 TIs when TR = 50 ms, respectively. The percent error of each tube is the difference between the T_1_5 and the corresponding T_1 in Table 1 divided by T_1 values in Table 1.